nature photonics

Article

https://doi.org/10.1038/s41566-024-01574-0

Inverted organic solar cells with an in situ-derived SiO_xN_y passivation layer and power conversion efficiency exceeding 18%

Received: 12 June 2024

Accepted: 21 October 2024

A list of authors and their affiliations appears at the end of the paper

Inverted organic solar cells are attractive for commercialization. However, their power conversion efficiency (PCE) still lags their conventional architecture counterpart. Here we propose a new approach to enhance the performance and stability of structure-inverted non-fullerene organic solar cells. We use an in situ-derived inorganic SiO_xN_y passivation layer, formed by curing a solution-deposited perhydropolysilazane thin film in ambient atmosphere on top of the commonly used ZnO transport layer. Oxygen vacancies and dangling bonds of ZnO create a doped region in the photoactive layer, leading to losses in photocurrent due to enhanced recombination of photogenerated holes within this region. The optimized SiO_xN_y interlayer effectively passivates the ZnO surface defects by forming Zn–O–Si bonds, leading to a vanishing doped region. At the same time, SiO_xN_y induces a preferential accumulation of the non-fullerene acceptor near the electron contact, which also favours charge extraction. The combination of both effects leads to increased photocurrent density and PCE, with certified PCE values of 18.49% and 18.06% for cells with active areas of 5.77 mm^2 and 100.17 mm^2, respectively, using PM6:L8-BO as the photoactive layer. Importantly, cells containing inorganic SiO_xN_y exhibit an estimated T_{80} lifetime of 24,700 h (where T_{80} is the time it takes for the PCE to drop to 80% of its initial value) under white light illumination, corresponding to an operational lifespan exceeding 16 years. The results underscore the potential of our approach for practical applications of highly efficient and stable inverted organic solar cells.

Organic solar cells (OSCs) are promising candidates for energy production due to their inherent flexibility[1,2], light weight[3] and compatibility with solution-based printing processes[4–6]. Recent advances in photoactive materials, including wide-bandgap conjugated polymer donors[7,8] and matched low-bandgap non-fullerene acceptors (NFAs)[9–14], have led to a remarkable increase in the power conversion efficiency (PCE), now over 20% (refs. 15–18). However, record PCEs are limited to a specific device design known as the conventional or standard structure, in which the photoactive layer is sandwiched between an electron transport layer (ETL) and a hole transport layer (HTL), arranged as a transparent electrode/HTL/active layer/ETL/metal electrode. For commercialization purposes, there is a growing interest in reversing this layer sequence so that the HTL is deposited on top of the photoactive layer. These so-called inverted OSCs offer the advantage that a high-work-function top electrode can be used, which ensures better compatibility with printing processes and improves long-term operational stability[19–22].

Despite these advantages, the efficiency of inverted OSCs still lags behind their conventional counterparts, whereas their stability is not

e-mail: qluo2011@sinano.ac.cn; Ronald.Osterbacka@abo.fi; cqma2011@sinano.ac.cn

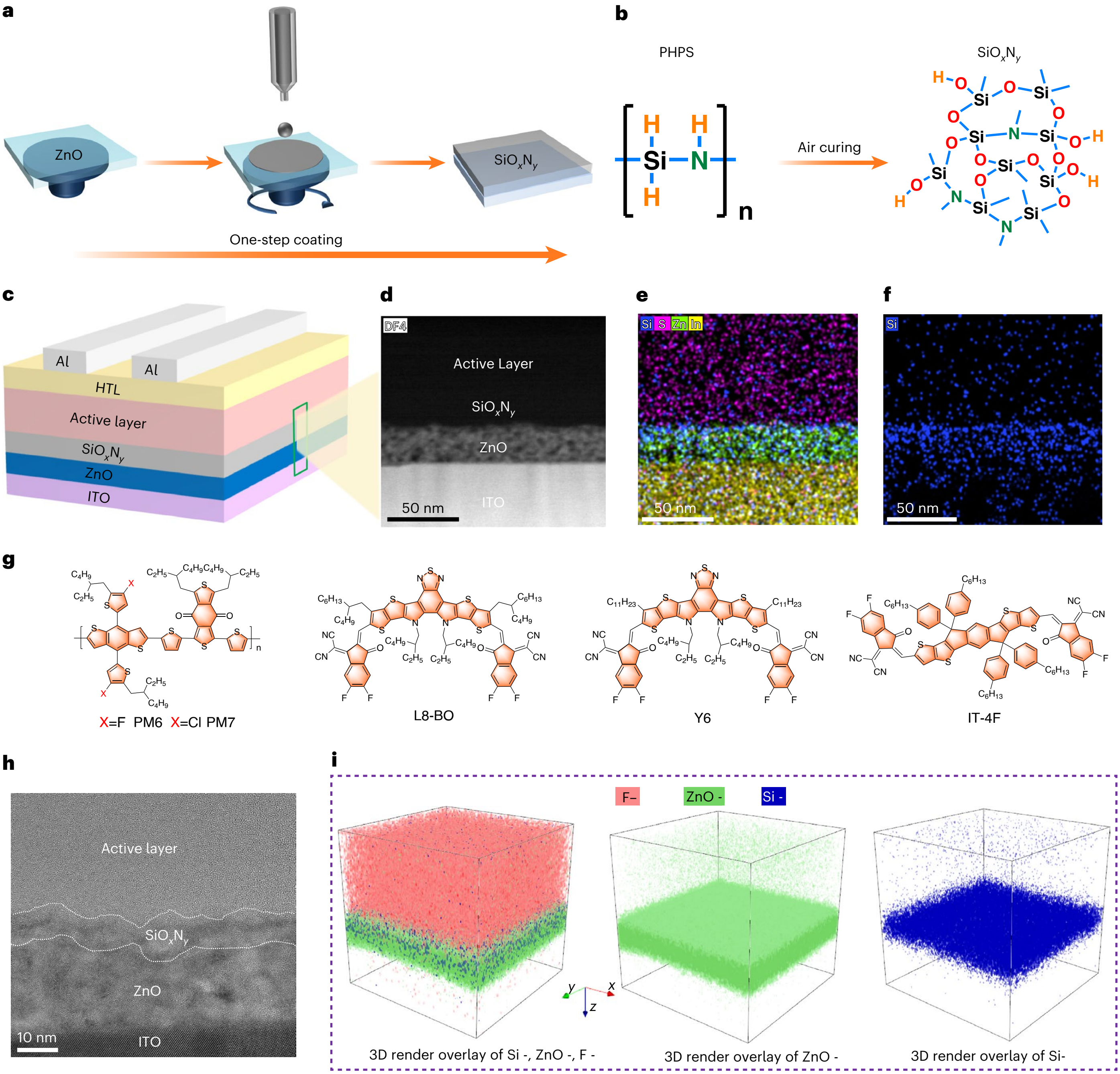

Fig. 1 | Realization of in situ-derived SiO_xN_y for inverted OSCs through solution deposition of PHPS and subsequent air curing. **a**, Illustration of the one-step coating processes for the preparation of a thin SiO_xN_y layer on top of ZnO. **b**, Conversion of PHPS to amorphous SiO_xN_y during air curing. **c**, Device structure of the inverted OSCs. **d**, Cross-sectional HR-STEM image of an ITO/ZnO/SiO_xN_y/PM6:Y6 sample. **e**, Combined EDX mapping of Si, S, Zn and In. **f**, Isolated EDX mapping of Si. **g**, Molecular structures of the organic semiconductors used in this study. **h**, Magnified cross-sectional HR-STEM image of an ITO/ZnO/SiO_xN_y/PM6:Y6 sample. **i**, Three-dimensional (3D) TOF-SIMS mapping of PM7:Y6 on ZnO/SiO_xN_y.

yet competitive with the benchmarks set by commercial silicon solar cells[21,23]. One issue regarding inverted OSCs is that they require ETLs that can be processed from solution on top of the transparent bottom electrode, typically made of highly conducting indium tin oxide (ITO). Commonly used ETLs include metal oxides such as zinc oxide (ZnO) (ref. 24), titania (TiO_2) (ref. 25) and tin oxide (SnO_2) (ref. 26). However, these materials are prone to surface defects, which inevitably cause interfacial charge recombination and limit device performance[27,28]. For instance, the unintentional n-doping of ZnO by oxygen vacancies or H ions[29] has been shown to cause undesired space-charge effects near the cathode, leading to considerable losses through interfacial recombination.

One promising approach to address these issues is passivating the metal oxide layer. Several organic passivating molecules, including fullerene derivatives[30], Lewis acids[19,22,31], ammonium salts[20] and even bioactive molecules[32,33], have been successfully utilized to modify the ETL. However, organic materials, including the organic active layer itself, are susceptible to photocatalytic decomposition at the ETL surface, leading to additional problems with long-term operational stability[21,34]. On the contrary, inert inorganic materials such as alumina

(Al_2O_3) (ref. 25), zirconia (ZrO_2) (ref. 35) and two-dimensional selenides[36] have proven to improve both device performance and stability in inverted OSCs, but mostly require vacuum deposition techniques like atomic layer deposition and are, thus, not compatible with solution processing.

In this study, we introduce an in situ-derived inorganic SiO_xN_y passivation layer that enables highly efficient and stable inverted OSCs. The SiO_xN_y layer, with an optimal thickness of ~2 nm, is prepared by curing a solution-deposited perhydropolysilazane (PHPS) film in ambient air at room temperature. When applied to an ETL of ZnO, we find that the reactive Si–H groups of PHPS effectively passivate the surface defects and reduce interface recombination. Moreover, the SiO_xN_y interlayer induces NFA enrichment at the ZnO interface, facilitating improved charge extraction. A combination of these effects result in exceptionally high PCEs of 18.55% and 18.12% for inverted PM6:L8-BO solar cells with an active area of 5.77 mm^2 and 100.17 mm^2, respectively, along with independently certified stabilized PCEs of 18.49% and 18.06%. Importantly, the highly efficient SiO_xN_y-passivated devices exhibit a long T_{80} lifetime of 24,700 h (T_{80} is the time it takes for the PCE to drop to 80% of its initial value) under continuous white light illumination, corresponding to an estimated operational lifespan of over 16 years.

Characterization of in situ-derived SiO_xN_y

Figure 1a depicts the preparation process for the in situ-derived SiO_xN_y thin films, where a PHPS solution in dibutyl ether (DBE) was spin coated onto the ZnO surface and cured in air at room temperature to convert PHPS into SiO_xN_y. PHPS is an inorganic polymer consisting of alternating nitrogen–silicon bonds that react with oxygen and/or water to generate amorphous SiO_xN_y at room temperature (Fig. 1b). During air curing, chemical reactions include the cleavage of Si–N bonds by water, yielding $R_3Si{-}NH_2$, $R_3Si{-}OH$ and ammonia (Supplementary Fig. 1)[37].

To verify successful SiO_xN_y deposition on ZnO, high-resolution scanning transmission electron microscopy (HR-STEM) was performed on a sample with the ITO/ZnO/SiO_xN_y/PM6:Y6 structure (Fig. 1c). Note that for these investigations, the SiO_xN_y layer was prepared from a 0.2 vol% PHPS solution, yielding thicker SiO_xN_y films than for the optimized solar cells discussed later. Figure 1d–f shows the HR-STEM image of a sample cross-section prepared with a focused ion beam alongside corresponding energy-dispersive X-ray (EDX) spectroscopy mappings of Si, S, Zn and In. More detailed mappings of the individual elements are shown in Supplementary Fig. 2. Together with the magnified transmission electron microscopy (TEM) image shown in Fig. 1h and Supplementary Fig. 3, an ~5 nm SiO_xN_y film can be clearly identified on top of the ~20 nm ZnO layer.

Further chemical imaging was done using time-of-flight secondary ion mass spectrometry (TOF-SIMS) on samples prepared from PHPS solutions with different concentrations. Both two-dimensional (Supplementary Fig. 4) and three-dimensional (Fig. 1i and Supplementary Fig. 5) elemental maps show a complete and homogeneous coverage of the ZnO layer with SiO_xN_y on a lateral scale of 50 µm as well as an increase in Si intensity with increasing PHPS concentration as expected for successful SiO_xN_y formation. Moreover, the TOF-SIMS maps indicate that SiO_xN_y not only covers the surface but also penetrates the voids within the nanocrystalline ZnO layer, as can also be seen from the isolated EDX signal for Si (Fig. 1f). Another important observation is the accumulation of F species at the interface between ZnO and the photoactive layer (Supplementary Fig. 2h). This points towards a vertical compositional gradient in the photoactive layer with a higher concentration of the Y6 acceptor near the ETL interface, which we ascribe to a pulling effect related to SiO_xN_y, as discussed in detail later.

Interactions of SiO_xN_y with ZnO and Y6

To investigate the interactions of SiO_xN_y with ZnO and Y6 in more detail, we performed X-ray photoelectron spectroscopy (XPS) measurements. As discussed in Supplementary Note 2, the measured Si2*p* and N1*s* spectra (Supplementary Fig. 6) further confirm the conversion of PHPS to SiO_xN_y at the ZnO surface. Figure 2a,b shows the high-resolution O1*s* and Zn2*p* XPS spectra of ZnO surfaces with and without PHPS treatment (for comparison, we also measured a ZnO film treated with the pure solvent DBE). As shown in Fig. 2a, two O1*s* signals peaking at 531.3 eV and 529.9 eV can be deconvoluted for the untreated ZnO, which we assign to surface-absorbed hydroxyl groups[38] and oxygen bonded to Zn atoms[39], respectively. After the deposition of SiO_xN_y, the O1*s* signal could be fitted to three peaks centred at 529.9 eV, 530.7 eV and 532.1 eV, corresponding to Zn–O–Zn, Zn–O–Si (ref. 40) and Si–O–Si (ref. 41), respectively. The disappearance of the 531.3 eV peak and the appearance of the 530.7 eV peak in the spectra demonstrate the conversion of surface hydroxyl groups to new Zn–O–Si bonds. Figure 2b shows how the Zn2*p* signals are shifted from 1,021.1 eV (Zn2$p_{3/2}$) and 1,044.2 eV (Zn2$p_{1/2}$) to 1,021.6 eV and 1,044.7 eV for the SiO_xN_y-treated samples. Together with the occurrence of a new peak at 940 cm^{-1} in Fourier-transform infrared spectroscopy (Supplementary Fig. 8) that corresponds to the formation of Zn–O–Si (ref. 42) bonds, the decreased ZnO defect-state emission[43] in the photoluminescence (PL) spectrum (Fig. 2e), we conclude that during air curing, the amino groups of PHPS react with the surface hydroxyl groups of ZnO, generating Zn–O–Si bonds (Fig. 2f).

Next, we focus on the interaction between SiO_xN_y and the NFA Y6. As shown in Fig. 2c,d and Supplementary Fig. 9, the Si2*p* signal is shifted from 102.1 eV to 102.7 eV after depositing a thin film of Y6 on ZnO/SiO_xN_y, whereas the F1*s* signal is shifted from 687.7 eV (related to the F–C bond of Y6 (ref. 44)) to 687.3 eV. These shifts indicate a strong interaction between SiO_xN_y and Y6 through Si···F–C bonds[45] (Supplementary Note 4 and Fig. 2j). Figure 2h,i depicts the TOF-SIMS depth profiles of PM6:Y6 films on ZnO and ZnO/SiO_xN_y surfaces. In particular, besides the high intensity of Si at the ETL interface, the ITO/ZnO/SiO_xN_y/PM6:Y6 sample exhibits a higher cyano (CN)/S ratio (5.5) than the ITO/ZnO/PM6:Y6 sample (3.4). Since the CN signal stems from Y6 and the S signal can be predominantly attributed to PM6, the increased CN/S ratio indicates a higher acceptor concentration close to the ZnO/SiO_xN_y surface, consistent with the accumulation of Y6 at the interface shown in the STEM measurements (Supplementary Fig. 2h). This accumulation is presumed to result from the formation of Si–F–C and hydrogen bonds between the Si–NH and the CN group of Y6 (as shown earlier). We could further verify the increased acceptor concentration at the ETL interface by using the alternative donor PM7, which contains the characteristic element Cl. As shown in Supplementary Fig. 10, the ITO/ZnO/SiO_xN_y sample shows a much increased CN/Cl ratio of 17.2 compared with 9.5 without SiO_xN_y passivation.

To gain deeper insights into the interactions between ZnO, SiO_xN_y and Y6, we performed density functional theory (DFT) calculations for a model of Y6, namely, 5,6-difluoro-1,1-dicyanomethylene-3-indanone (IC-2F) and examined its interaction with the ZnO(101) surface. The adsorption energy (E_{ad}) of the organic moiety to both ZnO and ZnO/SiO_xN_y surfaces was calculated and is listed in Fig. 2g and Supplementary Fig. 11. Our analysis reveals that IC-2F interacts with the hydroxyl group (–OH) through the C–F···H–O–Zn interaction, with an E_{ad} value of −0.75 eV. By contrast, IC-2F exhibits a strong interaction through Si···F–C, with an E_{ad} value of −1.64 eV. The stronger interaction with SiO_xN_y effectively brings the NFA molecule closer to the ZnO/SiO_xN_y surface. Additionally, atomic force microscopy (AFM) (Supplementary Fig. 13) and grazing-incidence wide-angle X-ray scattering measurements (Supplementary Fig. 14) showed the surface morphology and crystallinity of the photoactive layers (Supplementary Note 5), which indicates that SiO_xN_y has little effect on the crystallinity as well as the bulk morphology of the active layer.

Solar cell performance

Inverted OSCs were fabricated with a structure of ITO/ZnO/SiO_xN_y/active layer/MoO_3/Al (Fig. 1c). Initially, we used PM6:Y6 as a model

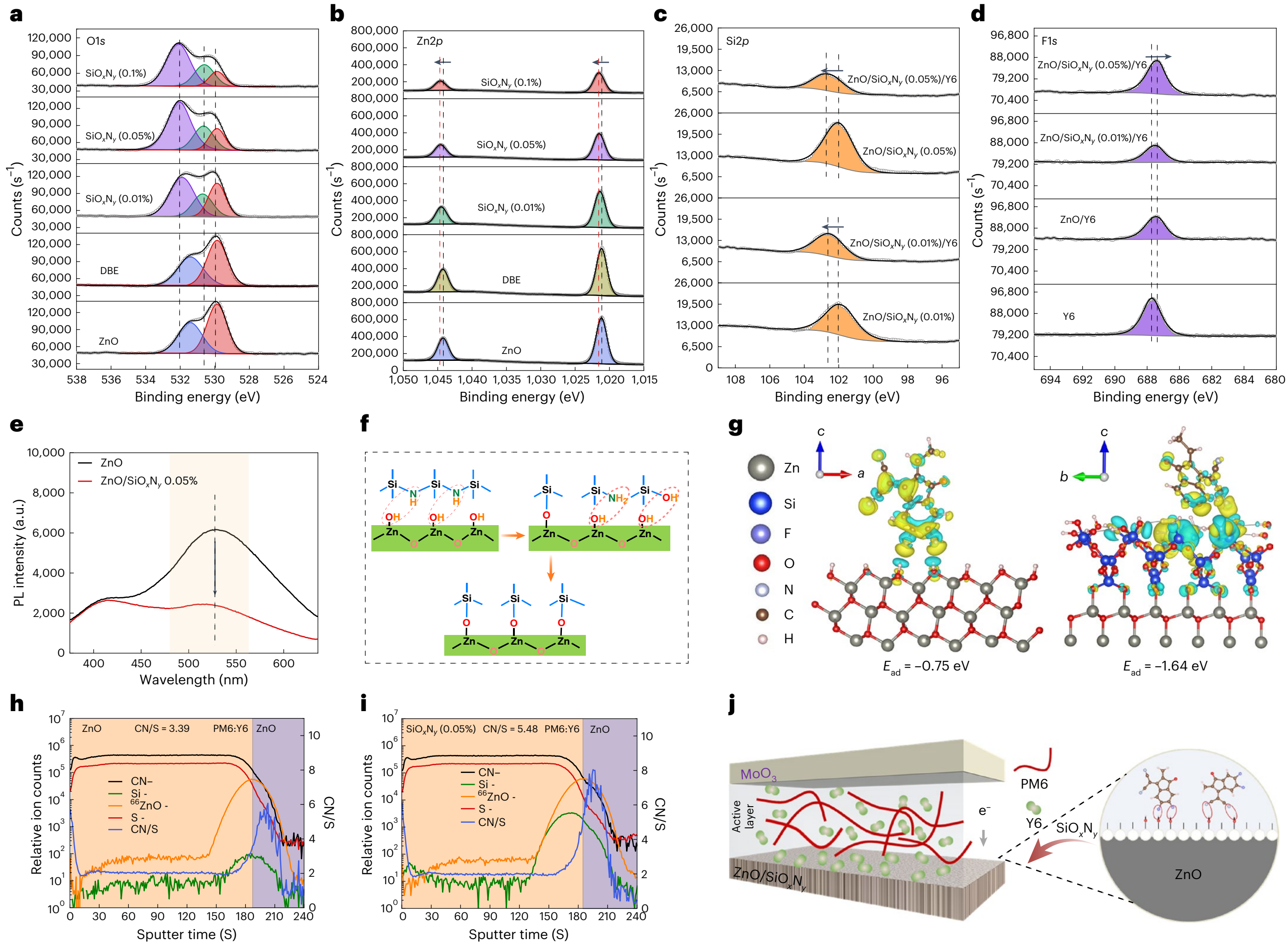

Fig. 2 | Interactions between ZnO, SiO_xN_y and Y6. a,**b**, XPS and fitted spectra of O1*s* (**a**) and Zn2*p* (**b**) for pristine ZnO and ZnO/SiO_xN_y films as a function of PHPS concentration. **c**,**d**, XPS spectra of Si2*p* (**c**) and F1*s* (**d**) for Y6 on ZnO and ZnO/SiO_xN_y surface as a function of PHPS concentration. **e**, PL of ZnO and ZnO/SiO_xN_y films excited with light at 340 nm under identical experimental conditions. **f**, Schematic of the chemical reaction between SiO_xN_y and ZnO. **g**, Charge density difference for Y6 on a ZnO(101) surface (left) and Y6 on a ZnO/SiO_xN_y surface (right), where E_{ad} is the adsorption energy calculated from DFT. Yellow/blue represents charge accumulation/depletion, where the isosurfaces refer to isovalues of 2.0×10^{-3} electrons bohr^{-3}. **h**,**i**, TOF-SIMS depth profiles of PM6:Y6-based devices prepared without (**h**) and with (**i**) a SiO_xN_y layer. **j**, Schematic of the interaction between ZnO/SiO_xN_y and Y6.

photoactive layer (Fig. 1g shows the chemical structures) to investigate the effect of SiO_xN_y passivation and optimize the SiO_xN_y layer thickness. As detailed in Supplementary Note 6, this passivation results in a slight improvement in the open-circuit voltage (V_{OC}) and fill factor (FF), but significantly enhances the short-circuit current (J_{SC}) of the devices (Supplementary Figs. 15 and 16). The device performance was found to be sensitive to the thickness of the SiO_xN_y layer, and an optimal 0.05 vol% PHPS solution was confirmed, which yields an optimal SiO_xN_y layer thickness in the range of 1–2 nm. Besides, we note that the SiO_x layer with different thicknesses made by atomic layer deposition on ZnO can significantly increase J_{SC} (Supplementary Fig. 17b and Supplementary Table 3), demonstrating the generality of surface defect passivation by SiO_x.

Next, we implemented optimized in situ-derived SiO_xN_y layers in solar cells utilizing PM6:Y6, PM6:L8-BO and PM6:IT-4F as the photoactive layer. Current density–voltage (*J*–*V*) characteristics of small-area devices are shown in Fig. 3a,b and Supplementary Fig. 18b, and the photovoltaic performance data are listed in Table 1. For all the three active layer blends, the incorporation of the SiO_xN_y layer increases the J_{SC} value by 1.0–1.5 mA cm^{-2}, resulting in an improvement in the PCE. We note that this improvement cannot be explained by a 'washing effect' of the DBE solvent used for preparing the SiO_xN_y layer by spin coating (Supplementary Fig. 19). Furthermore, we found that SiO_xN_y passivation has a similar positive effect even on devices in which ZnO was prepared using other preparation routines, including nanoparticles synthesized from dimethyl sulfoxide and the sol–gel method (Supplementary Fig. 20), which demonstrates the general applicability of the approach. With the optimized SiO_xN_y layer, we achieved the highest PCE of 18.55% for an inverted PM6:L8-BO solar cell with an active area of 5.77 mm^2, with an independently certified stabilized PCE of 18.49% (Fig. 3c). This represents one of the highest certified efficiencies reported so far among all the inverted OSCs (Supplementary Fig. 18d).

To identify the primary contributing factor to the increased PCE, particularly J_{SC}, we measured the external quantum efficiency (EQE) spectra. For all the photoactive materials studied here, the EQE shows an improvement over a wide range of wavelengths from 450 to 850 nm (Fig. 3d,e and Supplementary Fig. 15c). To exclude that this improvement is simply due to an increase in the active layer thickness, we measured the ultraviolet–visible absorption of PM6:Y6 films deposited on various SiO_xN_y layers (Supplementary Fig. 21) and performed a systematic thickness study of inverted PM6:Y6 solar cells (Supplementary Fig. 22). We found that the presence of SiO_xN_y has only an insignificant

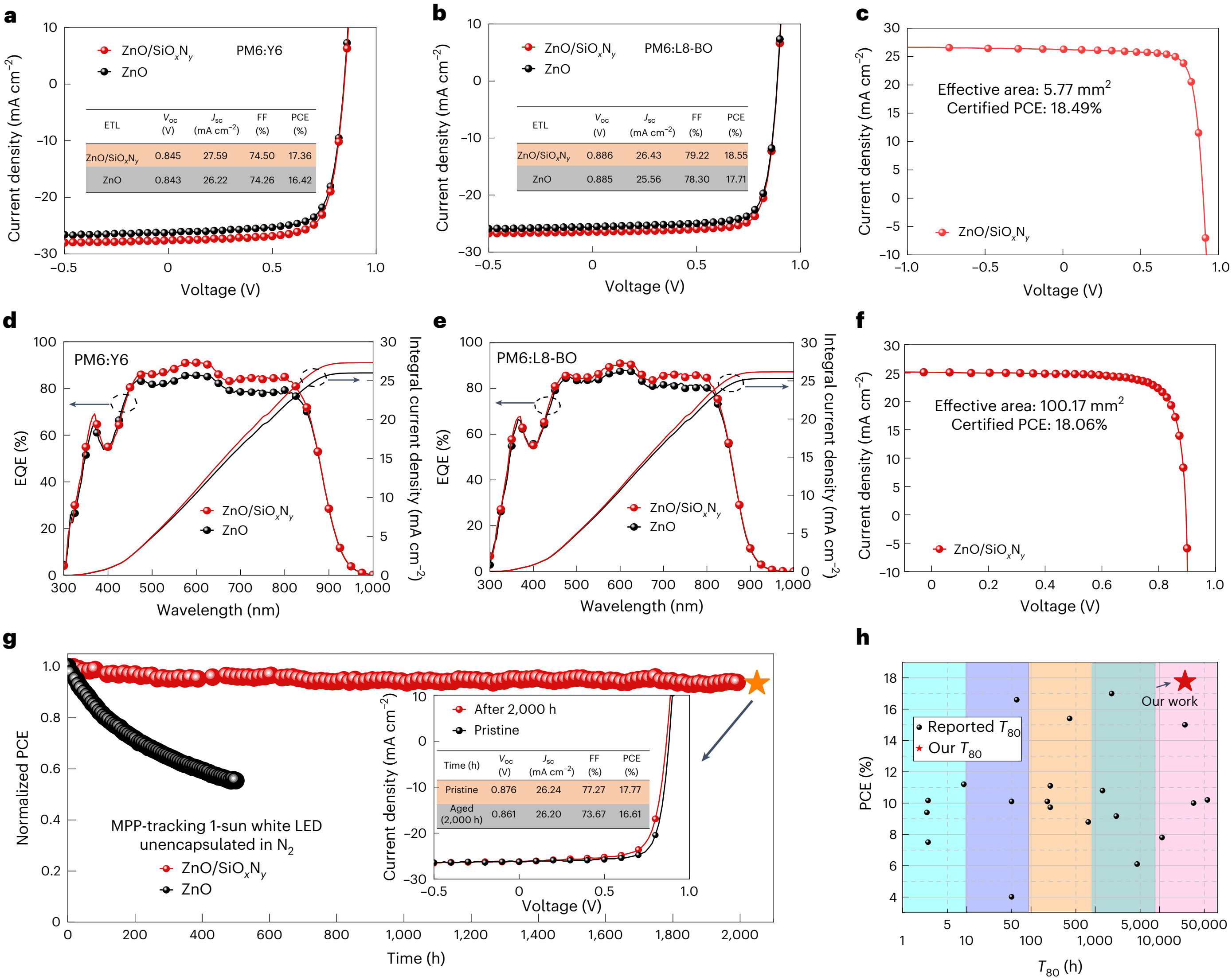

ETL	V_{oc} (V)	J_{sc} (mA cm^{-2})	FF (%)	PCE (%)
ZnO/SiO$_x$N$_y$	0.845	27.59	74.50	17.36
ZnO	0.843	26.22	74.26	16.42

ETL	V_{oc} (V)	J_{sc} (mA cm^{-2})	FF (%)	PCE (%)
ZnO/SiO$_x$N$_y$	0.886	26.43	79.22	18.55
ZnO	0.885	25.56	78.30	17.71

Time (h)	V_{oc} (V)	J_{sc} (mA cm^{-2})	FF (%)	PCE (%)
Pristine	0.876	26.24	77.27	17.77
Aged (2,000 h)	0.861	26.20	73.67	16.61

Fig. 3 | Performance of inverted OSCs with a SiO$_x$N$_y$-passivated ETL. **a**,**b**, *J*–*V* curves of ZnO and ZnO/SiO$_x$N$_y$ devices based on PM6:Y6 (**a**) and PM6:L8-BO (**b**) with an active area of 9 mm^2 and a mask area of 5.77 mm^2. **c**, *J*–*V* curve of a 5.77 mm^2 inverted PM6:L8-BO solar cell measured at SIMIT. **d**,**e**, Corresponding EQE curves of ZnO and ZnO/SiO$_x$N$_y$ devices based on PM6:Y6 (**d**) and PM6:L8-BO (**e**). **f**, *J*–*V* curve of a 100.17 mm^2 inverted PM6:L8-BO binary cell measured at SIMIT. **g**, Long-term operational stability of OSCs with and without SiO$_x$N$_y$ at the maximum power point (MPP) tracking under continuous illumination using a white LED with light intensity equivalent to 1 sun in a N$_2$-filled glove box. The initial PCEs for the ZnO and ZnO/SiO$_x$N$_y$ solar cells were 16.90% ± 0.1% and 17.60% ± 0.1%, respectively. The inset shows the *J*–*V* curves of the best-performing cell before and after 2,000 h of aging, which showed an initial PCE of 17.77% and a final PCE of 16.61%. **h**, Performance–lifetime comparison of our results (red stars) and reported results in the literature (black dots) of selected OSCs. The photovoltaic data and the corresponding references are included in Supplementary Table 14.

influence on the absorption properties of PM6:Y6 and that the decreasing trend of the FF with increasing PM6:Y6 layer thickness (Supplementary Fig. 23) is in contradiction with the observed slight increase on SiO$_x$N$_y$ passivation. Thus, we conclude that the increase in J_{SC} does not result from an increase in the active layer thickness (Supplementary Note 8) but from the passivation effect of SiO$_x$N$_y$ through forming Zn–O–Si bonds combined with the favourable accumulation of NFA molecules near the ETL interface (as shown earlier). Our hypothesis that surface passivation, which leads to reduced interface recombination, is the main reason for the improved device performance is supported by a series of additional electro-optical measurements (Supplementary Note 9 and Supplementary Figs. 24 and 25) as well as the device simulations discussed in the next section.

In addition to enhancing performance, the SiO$_x$N$_y$ surface treatment was also found to improve the reproducibility of the inverted solar cells. Supplementary Fig. 26b shows the PCE histogram for a series of PM6:L8-BO devices utilizing SiO$_x$N$_y$, peaking at 18% and with a particularly narrower distribution compared with control devices having untreated ZnO as the ETL. We attribute this improvement to the lower surface free energy of ZnO treated with SiO$_x$N$_y$ (as shown earlier), resulting in a smoother surface morphology confirmed by AFM, TEM and two-dimensional TOF-SIMS measurements across various lateral scales (Supplementary Note 10 and Supplementary Figs. 27–29). All the characterization methods show excellent homogeneity of ZnO/SiO$_x$N$_y$ surfaces up to 100 µm, making them promising for large-area devices. To demonstrate this, we fabricated PM6:L8-BO solar cells with an active area of 1 and 4 cm^2 (Supplementary Fig. 30 shows the *J*–*V* curves), yielding champion PCEs of 18.12% and 17.14%, respectively. Interestingly, both increase in V_{OC} (0.884 V versus 0.881 V for 1 cm^2 and 0.878 V versus 0.867 V for 4 cm^2 devices) and the FF were even more pronounced for the larger-area device, showcasing the excellent surface passivation capability of SiO$_x$N$_y$ on size scales relevant for the mass production

Table 1 | Photovoltaic parameters of PM6:Y6, PM6:L8-BO and PM6:IT-4F inverted solar cells with and without SiO_xN_y under AM1.5G

ETL	Active layer	V_{OC} (V)	J_{SC} (mA cm^{-2})	J_{SC}^{EQE} (mA cm^{-2})[a]	FF (%)	PCE (%)[b]
ZnO/SiO_xN_y	PM6:Y6	0.845 (0.842 ± 0.002)	27.59 (27.16 ± 0.38)	27.32	74.50 (74.08 ± 0.36)	17.36 (16.95 ± 0.30)
ZnO		0.843 (0.841 ± 0.002)	26.22 (25.55 ± 0.35)	26.00	74.26 (74.36 ± 0.15)	16.42 (15.98 ± 0.23)
ZnO/SiO_xN_y	PM6:L8-BO	0.886 (0.888 ± 0.003)	26.43 (26.38 ± 0.06)	26.18	79.22 (78.69 ± 0.24)	18.55 (18.43 ± 0.06)
ZnO		0.885 (0.884 ± 0.002)	25.56 (25.33 ± 0.15)	25.31	78.30 (78.22 ± 0.18)	17.71 (17.51 ± 0.11)
ZnO/SiO_xN_y	PM6:IT-4F	0.830 (0.830 ± 0.003)	21.74 (21.37 ± 0.26)	21.43	71.16 (70.54 ± 0.70)	12.84 (12.51 ± 0.23)
ZnO		0.829 (0.824 ± 0.004)	20.63 (20.46 ± 0.21)	20.35	70.48 (70.26 ± 0.16)	12.05 (11.85 ± 0.20)

[a] J_{SC} calculated by convoluting the spectral response (EQE) under AM1.5G spectrum. [b] The average parameters were calculated from eight individual devices and the errors correspond to the standard deviation.

of OSCs. The 1 cm^2 cell was independently certified by a third party, achieving a PCE of 18.06% (Fig. 3f). To our knowledge, this represents the first instance of an inverted OSC surpassing an efficiency of 18% at an active area of 1 cm^2.

To assess the stability of the SiO_xN_y-passivated devices, we recorded their performance under continuous white light-emitting diode (LED) illumination in an inert atmosphere. Figure 3g illustrates the PCE decay curves, with complete decay traces provided in Supplementary Fig. 31. Although the reference ZnO/PM6:L8-BO solar cells lost 55% of their PCE already after 500 h (92% for V_{OC}, 75% for J_{SC} and 80% for the FF), the ZnO/SiO_xN_y-based devices retained 94% of the initial PCE after aging for 2,000 h. Figure 3c (inset) shows the J–V curve of the aged solar cell, yielding remarkably high values of V_{OC} (0.861 V, 98% remaining), J_{SC} (26.20 mA cm^{-2}, 99% remaining) and the FF (73.67%, 95% remaining). In particular, the exceptional stability of J_{SC} is noteworthy, suggesting that the SiO_xN_y passivation effectively inhibits NFA decomposition at the ZnO interface, which is supported by light bleaching tests (Supplementary Fig. 32 and Supplementary Note 11). The slight decays observed in V_{OC} and the FF may be attributed to interfacial degradation at the polymer–MoO_3 interface[46,47], which is currently under investigation by our group. By fitting the linear decay after the initial 'burn-in', we estimate T_{80} to be 24,700 h, corresponding to a lifetime of over 16 years (assuming an average of 4 h of illumination time per day). Compared with previous work using an organic passivation layer of 2-phenylethanethiol (ref. 34), where the device PCE decreased from 17.07% to 15.48% after aging for 1,500 h in an inert atmosphere (Supplementary Fig. 33), this represents a great improvement in long-term stability. With a T_{80} lifetime of over 20,000 h (Supplementary Figs. 34 and 35) and an initial PCE of about 18%, the SiO_xN_y-passivated inverted PM6:L8-BO devices rank among the best-performing OSCs reported so far (Fig. 3h).

Effect of the SiO_xN_y layer

The primary effect of the SiO_xN_y layer (in freshly prepared devices) is to increase J_{SC}, suggesting that there is a substantial photocurrent loss present in inverted solar cells without SiO_xN_y. We attribute the photocurrent loss to the combined effect of the rough ZnO–active layer interface and the presence of donor-type defects in ZnO. As shown in Fig. 4a, this gives rise to a narrow, effectively n-doped interfacial region within the active layer at the ZnO surface (compensating for positively charged defects). On the basis of the surface roughness of ZnO, we estimate the width of this region to be on the order of 10–15 nm (Supplementary Fig. 27). The PL peak at around 530 nm, clearly visible in untreated ZnO films (Fig. 2e), is attributed to oxygen vacancies[29], which—together with hydrogen—are believed to be the predominant donor-type defects in ZnO (refs. 48,49). Conversely, the SiO_xN_y layer passivates the defects at the ZnO surface, reducing the effective n-doping within the interfacial bulk heterojunction region (Fig. 4b). This is evidenced by the suppressed PL from defects observed for ZnO/SiO_xN_y films in Fig. 2e and the fact that PHPS reacts with surface hydroxyl groups in ZnO (releasing hydrogen). The de-doping effect is further supported by the charge extraction by linearly increased voltage measurements, showing a decreased capacitance for devices with SiO_xN_y (Supplementary Fig. 40e,f).

To substantiate the passivation of defects as the primary origin of the enhanced solar cell performance, we next used electro-optical device simulations on inverted PM6:Y6 solar cells. For this purpose, a numerical one-dimensional drift–diffusion model, coupled to an optical transfer-matrix model, was utilized[50,51]. In the simulations, the higher acceptor content near the ZnO interface for passivated devices (see above) is implemented as an improved electron selectivity at the cathode contact. Otherwise, devices with and without SiO_xN_y are treated as identical, but with the latter having a thin n-doped region near the cathode contact (Methods). In this aspect, our model is similar to a recently proposed one to explain the enhanced J_{SC} obtained by passivating an HTL of PEDOT:PSS in standard NFA-based solar cells[52].

Figure 4c shows the simulated spatially resolved collection efficiency $\eta_{col}(x)$ of an inverted PM6:Y6 device with a 15-nm-thick n-doped region near the active layer–cathode contact, corresponding to the case without SiO_xN_y. The presence of the doped region gives rise to a screened electric field and increased electron density (Supplementary Fig. 41a–c), manifesting as the enhanced recombination of photogenerated holes and reduced η_{col} within this region. The subsequent loss of charge carriers photogenerated in this region, primarily originating from photons with wavelengths between 500 nm and 800 nm (Supplementary Fig. 41d), ultimately results in reduced J_{SC}. Conversely, removing the doped region, corresponding to the passivated device (with SiO_xN_y) and simulated in Fig. 4d (no doping), reduces losses due to recombination near the cathode contact, increasing J_{SC} in the process (Supplementary Fig. 41e). The corresponding simulated J–V curves at 1 sun illumination and EQE spectra are shown in Fig. 4e,f, respectively. The simulations (solid lines) accurately reproduce the experimental J–V curves (symbols) and EQE behaviour (Fig. 3d), suggesting that the increased J_{SC} is due to SiO_xN_y passivating defects at ZnO.

We note that optical interference effects can be excluded as a source for the increased J_{SC}, owing to nearly identical absorbance spectra (Supplementary Fig. 21) and thicknesses of the active layer. Similarly, changes in surface recombination and energy-level alignment at the contact is expected to mainly influence V_{OC} (ref. 53), playing a negligible role for J_{SC} (ref. 52). The higher FF and V_{OC} values of the

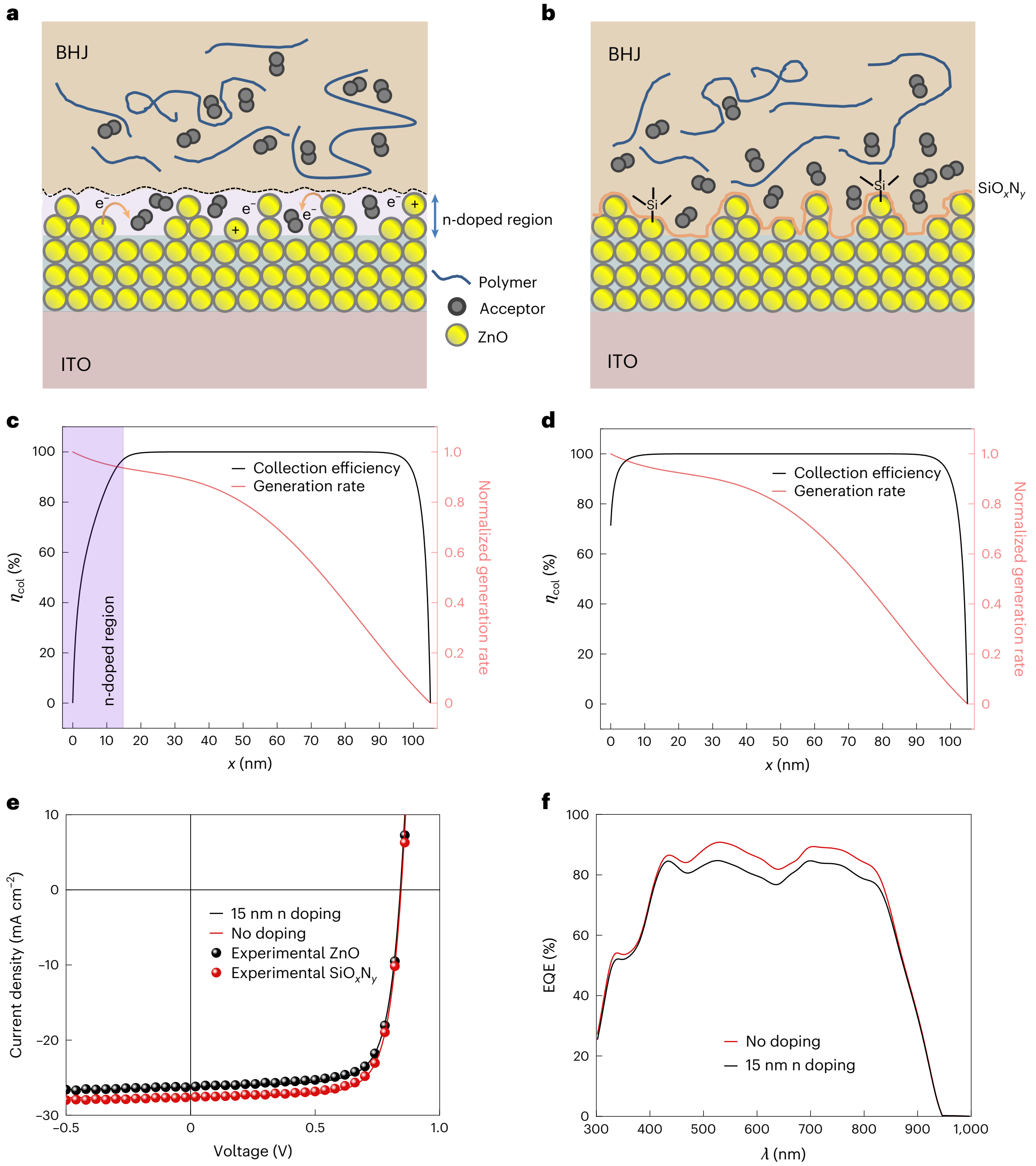

Fig. 4 | Electronic properties of the SiO$_x$N$_y$ OSCs. a,**b**, Schematic of the n-doped region inside the active layer at the ETL interface. BHJ, bulk heterojunction. **c**,**d**, Simulated charge collection efficiencies, $\eta_{col}(x)$, at short circuit as a function of position x inside the active layer. For comparison, the simulated (normalized (norm.)) generation rate profiles of the photogenerated charge carriers inside the active layer have been included. **e**, Experimental (symbols) J–V curves with or without SiO$_x$N$_y$ and simulated (solid lines) J–V characteristics with or without the n-doped region inside the active layer at the ETL interface. **f**, Simulated EQE with or without an n-doped region inside the active layer at the ETL interface.

passivated devices are assigned to the improved selectivity induced by the higher acceptor content near the passivated ZnO contact (Supplementary Fig. 41f). Devices with SiO$_x$N$_y$ also exhibit lower leakage currents in the dark (Supplementary Fig. 24d), indicative of a larger shunt resistance. The combined effects of a passivated ZnO surface, enhanced selectivity and larger shunt resistance explains the superior large-area and long-term device performance for inverted OSCs with a passivating SiO$_x$N$_y$ layer.

Conclusions

We have introduced and validated a novel in situ-derived SiO$_x$N$_y$ passivation layer for inverted OSCs, aimed at effectively passivating interface defects related to the ETL. Utilizing an inorganic PHPS precursor solution, we fabricated ultrathin SiO$_x$N$_y$ layers through a straightforward air curing process. Experimental confirmation of Zn–O–Si–F formation at the ETL–active layer interface highlights the successful chemical passivation of ZnO defects, along with a beneficial NFA enrichment at the ZnO interface. With this tailored SiO$_x$N$_y$ layer, we achieved certified PCEs of 18.49% and 18.06% for inverted PM6:L8-BO solar cells with an active area of 5.77 mm^2 and 100.17 mm^2, respectively. These results mark some of the highest reported efficiencies for inverted OSCs so far, particularly the first certified PCEs exceeding 18% for 1 cm^2 OSCs. Importantly, the SiO$_x$N$_y$-passivated PM6:L8-BO solar cells demonstrated exceptional long-term stability, maintaining the highest PCE even after a 2,000 h stability test. Overall, our study introduces a pioneering concept of utilizing solution-processed inorganic precursors to fabricate stable and efficient passivation layers for OSCs.

Online content

Any methods, additional references, Nature Portfolio reporting summaries, source data, extended data, supplementary information, acknowledgements, peer review information; details of author contributions and competing interests; and statements of data and code availability are available at https://doi.org/10.1038/s41566-024-01574-0.

References

1. Cheng, Y.-B., Pascoe, A., Huang, F. & Peng, Y. Print flexible solar cells. *Nature* **539**, 488–489 (2016).
2. Service, R. F. Solar energy gets flexible. *Science* **378**, 588–591 (2022).
3. Kaltenbrunner, M. et al. Ultrathin and lightweight organic solar cells with high flexibility. *Nat. Commun.* **3**, 770 (2012).
4. Zhang, K. et al. Toward solution-processed high-performance polymer solar cells: from material design to device engineering. *Chem. Mater.* **29**, 141–148 (2017).
5. Meng, L. et al. Organic and solution-processed tandem solar cells with 17.3% efficiency. *Science* **361**, 1094–1098 (2018).
6. Jiang, Y. et al. An alcohol-dispersed conducting polymer complex for fully printable organic solar cells with improved stability. *Nat. Energy* **7**, 352–359 (2022).
7. Zhao, W. et al. Molecular optimization enables over 13% efficiency in organic solar cells. *J. Am. Chem. Soc.* **139**, 7148–7151 (2017).
8. Fu, H., Wang, Z. & Sun, Y. Polymer donors for high-performance non-fullerene organic solar cells. *Angew. Chem. Int. Ed.* **58**, 4442–4453 (2019).
9. Hou, J., Inganäs, O., Friend, R. H. & Gao, F. Organic solar cells based on non-fullerene acceptors. *Nat. Mater.* **17**, 119–128 (2018).
10. Yuan, J. et al. Single-iunction organic solar cell with over 15% efficiency using fused-ring acceptor with electron-deficient core. *Joule* **3**, 1140–1151 (2019).
11. Liang, Y. et al. Organic solar cells using oligomer acceptors for improved stability and efficiency. *Nat. Energy* **7**, 1180–1190 (2022).
12. Yao, Z. et al. Complete peripheral fluorination of the small-molecule acceptor in organic solar cells yields efficiency over 19%. *Angew. Chem. Int. Ed.* **62**, e202312630 (2023).
13. Cheng, P., Li, G., Zhan, X. & Yang, Y. Next-generation organic photovoltaics based on non-fullerene acceptors. *Nat. Photon.* **12**, 131–142 (2018).
14. Li, C. et al. Non-fullerene acceptors with branched side chains and improved molecular packing to exceed 18% efficiency in organic solar cells. *Nat. Energy* **6**, 605–613 (2021).
15. Sun, Y. et al. π-Extended nonfullerene acceptor for compressed molecular packing in organic solar cells to achieve over 20% efficiency. *J. Am. Chem. Soc.* **146**, 12011–12019 (2024).
16. Guan, S. et al. Self-assembled interlayer enables high-performance organic photovoltaics with power conversion efficiency exceeding 20%. *Adv. Mater.* **36**, 2400342 (2024).
17. Chen, Z. et al. 20.2% efficiency organic photovoltaics employing a π-extension quinoxaline-based acceptor with ordered arrangement. *Adv. Mater.* **36**, 2406690 (2024).
18. Jiang, Y. et al. Non-fullerene acceptor with asymmetric structure and phenyl-substituted alkyl side chain for 20.2% efficiency organic solar cells. *Nat. Energy* **9**, 975–986 (2024).
19. Suo, Z. et al. An efficient interface modification material for improved efficiency and stability in inverted organic solar cells. *Mater. Chem. Front.* **8**, 562–566 (2024).
20. Xin, Y. et al. Multiarmed aromatic ammonium salts boost the efficiency and stability of inverted organic solar cells. *J. Am. Chem. Soc.* **146**, 3363–3372 (2024).
21. Duan, L. & Uddin, A. Progress in stability of organic solar cells. *Adv. Sci.* **7**, 1903259 (2020).
22. Li, S. et al. Achieving over 18% efficiency organic solar cell enabled by a ZnO-based hybrid electron transport layer with an operational lifetime up to 5 years. *Angew. Chem. Int. Ed.* **61**, e202207397 (2022).
23. Feldmann, F., Bivour, M., Reichel, C., Hermle, M. & Glunz, S. W. Passivated rear contacts for high-efficiency n-type Si solar cells providing high interface passivation quality and excellent transport characteristics. *Sol. Energy Mater. Sol. Cells* **120**, 270–274 (2014).
24. Huang, J., Yin, Z. & Zheng, Q. Applications of ZnO in organic and hybrid solar cells. *Energy Environ. Sci.* **4**, 3861–3877 (2011).
25. Vasilopoulou, M. et al. Atomic-layer-deposited aluminum and zirconium oxides for surface passivation of TiO_2 in high-efficiency organic photovoltaics. *Adv. Energy Mater.* **4**, 1400214 (2014).
26. Jiang, Y. Y. et al. Photocatalytic effect of ZnO on the stability of nonfullerene acceptors and its mitigation by SnO_2 for nonfullerene organic solar cells. *Mater. Horiz.* **6**, 1438–1443 (2019).
27. Yu, R. et al. Efficient interface modification via multi-site coordination for improved efficiency and stability in organic solar cells. *Energy Environ. Sci.* **15**, 822–829 (2022).
28. Wang, Y. et al. New method for preparing ZnO layer for efficient and stable organic solar cells. *Adv. Mater.* **35**, 2208305 (2023).
29. Bandopadhyay, K. & Mitra, J. Zn interstitials and O vacancies responsible for n-type ZnO: what do the emission spectra reveal? *RSC Adv.* **5**, 23540–23547 (2015).
30. Li, Y. et al. Non-fullerene acceptor organic photovoltaics with intrinsic operational lifetimes over 30 years. *Nat. Commun.* **12**, 5419 (2021).
31. Han, Y. et al. An efficiency of 16.46% and a T_{80} lifetime of over 4,000 h for the PM6:Y6 inverted organic solar cells enabled by surface acid treatment of the zinc oxide electron transporting layer. *ACS Appl. Mater. Interfaces* **13**, 17869–17881 (2021).
32. Liu, B.-W. et al. ZnO surface passivation with glucose enables simultaneously improving efficiency and stability of inverted polymer:non-fullerene solar cells. *Chinese J. Polym. Sci.* **40**, 1594–1603 (2022).
33. Zhao, Y. et al. Achieving sustainability of greenhouses by integrating stable semi-transparent organic photovoltaics. *Nat. Sustain.* **6**, 539–548 (2023).
34. Liu, B. et al. Simultaneously achieving highly efficient and stable polymer:non-fullerene solar cells enabled by molecular structure optimization and surface passivation. *Adv. Sci.* **9**, 2104588 (2022).
35. Polydorou, E. et al. Improved stability of polymer solar cells in ambient air via atomic layer deposition of ultrathin dielectric layers. *Adv. Mater. Interfaces* **4**, 1700231 (2017).
36. Tan, J. et al. A ZnO&GeSe composite electron transport layer for organic solar cells. *J. Mater. Chem. A* **12**, 1530–1542 (2024).
37. Zhang, Z. et al. Hydrophobic, transparent and hard silicon oxynitride coating from perhydropolysilazane. *Polym. Int.* **64**, 971–978 (2015).
38. Coppa, B., Davis, R. & Nemanich, R. Gold Schottky contacts on oxygen plasma-treated, n-type ZnO (0001). *Appl. Phys. Lett.* **82**, 400–402 (2003).
39. Sun, Y., Seo, J. H., Takacs, C. J., Seifter, J. & Heeger, A. J. Inverted polymer solar cells integrated with a low-temperature-annealed sol-gel-derived ZnO film as an electron transport layer. *Adv. Mater.* **23**, 1679–1683 (2011).
40. Liu, Y. et al. Effects of amorphous-zinc-silicate-catalyzed ozonation on the degradation of *p*-chloronitrobenzene in drinking water. *Appl. Catal. A Gen.* **403**, 112–118 (2011).
41. JangJian, S.-K. & Wang, Y.-L. Bonding configuration and electrical properties of nitrogen and fluorine incorporated SiOC:H thin film

prepared by plasma enhanced chemical vapor deposition. *Surf. Coat. Tech.* **200**, 3140–3144 (2006).
42. Roy, A. et al. First preparation of nanocrystalline zinc silicate by chemical vapor synthesis using an organometallic single-source precursor. *Chem. Eur. J.* **10**, 1565–1575 (2004).
43. Polydorou, E. et al. Insights into the passivation effect of atomic layer deposited hafnium oxide for efficiency and stability enhancement in organic solar cells. *J. Mater. Chem. C* **6**, 8051–8059 (2018).
44. Hu, Q. et al. Improving efficiency and stability of perovskite solar cells enabled by a near-infrared-absorbing moisture barrier. *Joule* **4**, 1575–1593 (2020).
45. Sen, S. S. & Roesky, H. W. Silicon-fluorine chemistry: from the preparation of SiF_2 to C–F bond activation using silylenes and its heavier congeners. *Chem. Commun.* **54**, 5046–5057 (2018).
46. Doumon, N. Y. et al. Energy level modulation of ITIC derivatives: effects on the photodegradation of conventional and inverted organic solar cells. *Org. Electron.* **69**, 255–262 (2019).
47. Gu, H. et al. Revealing the interfacial photoreduction of MoO_3 with P3HT from the molecular weight-dependent 'burn-in' degradation of P3HT:$PC_{61}BM$ solar cells. *ACS Appl. Energ. Mater.* **3**, 9714–9723 (2020).
48. Janotti, A. & Van de Walle, C. G. Fundamentals of zinc oxide as a semiconductor. *Rep. Prog. Phys.* **72**, 126501 (2009).
49. Wilken, S., Parisi, J. R. & Borchert, H. Role of oxygen adsorption in nanocrystalline ZnO interfacial layers for polymer–fullerene bulk heterojunction solar cells. *J. Phys. Chem. C* **118**, 19672–19682 (2014).
50. Nyman, M. et al. Requirements for making thick junctions of organic solar cells based on nonfullerene acceptors. *Sol. RRL* **5**, 2100018 (2021).
51. Li, W. et al. Organic solar cells with near-unity charge generation yield. *Energy Environ. Sci.* **14**, 6484–6493 (2021).
52. Kim, Y. R. et al. Mitigating detrimental effect of self-doping near the anode in highly efficient organic solar cells. *Adv. Funct. Mater.* **33**, 2300147 (2023).
53. Phuong, L. Q. et al. Quantifying quasi-Fermi level splitting and open-circuit voltage losses in highly efficient nonfullerene organic solar cells. *Sol. RRL* **5**, 2000649 (2021).

Bowen Liu [1,2,3], **Oskar J. Sandberg** [4], **Jian Qin** [1,2], **Yueying Liu** [5], **Sebastian Wilken** [4], **Na Wu** [1], **Xuelai Yu** [1,2], **Jin Fang** [1], **Zhiyun Li** [6], **Rong Huang** [6], **Wusong Zha** [1,2], **Qun Luo** [1,2] ✉, **Hongwei Tan** [5], **Ronald Österbacka** [1,4] ✉ **& Chang-Qi Ma** [1,2] ✉

[1]i-Lab & Printable Electronics Research Center, Suzhou Institute of Nano-Tech and Nano-Bionics, Chinese Academy of Sciences, Suzhou, People's Republic of China. [2]School of Nano-Tech and Nano-Bionics, University of Science and Technology of China, Hefei, People's Republic of China. [3]College of Chemistry and Molecular Sciences, Henan University, Kaifeng, People's Republic of China. [4]Physics and Center for Functional Materials, Faculty of Science and Engineering, Åbo Akademi University, Turku, Finland. [5]College of Chemistry, Beijing Normal University, Beijing, People's Republic of China. [6]Vacuum Interconnected Nanotech Workstation (Nano-X), Suzhou Institute of Nano-Tech and Nano-Bionics, Chinese Academy of Sciences, Suzhou, People's Republic of China. ✉e-mail: qluo2011@sinano.ac.cn; Ronald.Osterbacka@abo.fi; cqma2011@sinano.ac.cn

Methods

Materials

PM6 (PBDB-T-2F), IT-4F, Y6 and L8-BO were purchased from Solarmer Materials. PHPS was purchased from Iota Silicone Oil at a concentration of 20 wt% in DBE. DBE and methanol (MeOH) were purchased from Macklin Biochemical. $Zn(OAc)_2$, TMAH and KOH were purchased from J&K Scientific. 1,8-Diiodooctane and 1-chloronaphthalene were purchased from Sigma-Aldrich. 1,4-Diiodobenzene was purchased from TCI. Molybdenum(VI) oxide (MoO_3) was purchased from Strem Chemicals. All materials were used as received without further purification. ZnO nanoparticle solution was prepared through the reaction between KOH and $Zn(OAc)_2$ in MeOH (ref. 54). Dimethyl sulfoxide–ZnO was prepared through the reaction between TMAH and $Zn(OAc)_2$ in dimethyl sulfoxide[55].

Instruments and measurement

The cross-sections of the films on ITO substrates were obtained by a focused ion beam (FEI Helios 5UX) instrument. The film surface was covered with Au to facilitate positioning when preparing the cross-sections. The cross-sections of the film on ITO substrates were characterized with a TEM instrument (FEI F200X) coupled with an EDX spectrometer (Super-X). TEM measurements were performed using the commercial software Velox (v. 2.14.0.703-125f3e7193). The XPS spectra were measured using an ESCALAB 250Xi$^+$ spectrometer with a monochromatic Al Kα X-ray source with an overall energy space of $\Delta E = 0.1$ eV (the Vacuum Interconnected Nanotech Workstation (Nano-X), Suzhou Institute of Nano-Tech and Nano-Bionics), and the spectrum was referenced using the C–C-bound component of adventitious carbon. Ultraviolet photoelectron spectroscopy (UPS) was performed using a PHI 5000 VersaProbe III device with a He I source (21.22 eV) under an applied negative bias of 9.0 V and no applied negative bias for the secondary electron cut-off and Fermi edge. Inverse photoemission spectroscopy was performed using a PHI 5000 VersaProbe III instrument with low-energy electrons (8 V, 3 A). UPS and inverse photoemission spectroscopy data were processed using the commercial software PHI SmartSoft (v. 3.2.0.52). XPS and UPS were analysed by commercial software Thermo Avantage (v. 5.9921). TOF-SIMS mapping of the active layers was obtained using the ToF-SIMS5-100 instrument and commercial software SurfaceLab (v. 6). Grazing-incidence wide-angle X-ray scattering measurements were characterized by the Xeuss SAXS/WAXS 3.0 system (Xenocs) with an X-ray wavelength of 1.54189 Å at Nano-X. The surface roughness of the samples was analysed by AFM with a probe-type Park XE-120 microscope at room temperature. The ultraviolet–visible absorption and transmittance spectra of ZnO and NFA films were measured with a PerkinElmer Lambda 750 instrument at room temperature and all the films were spin coated on glass substrates and aged in a glove box under white LED illumination.

Theoretical calculations

All the DFT calculations were performed using the Vienna ab initio simulation package (v. 5.4.4) with the projector augmented wave method, and the Perdew–Burke–Ernzerhof functional within the generalized gradient approximation was used to describe the electronic exchange–correlation interaction. All the spin-polarized DFT calculations were performed using the Vienna ab initio simulation package with dispersion correction (DFT + D3). The interaction between core electrons and valence electrons was implemented through the projector augmented wave method, and the energy cut-off was set to 450 eV for the plane-wave basis sets. The Perdew–Burke–Ernzerhof functional within the generalized gradient approximation was used to describe the electronic exchange–correlation interaction. The following valence configurations were used in this work: $3d^{10}4p^2$ for Zn, $2s^22p^4$ for O, $2s^22p^2$ for C, $2s^22p^3$ for N, $3s^23p^2$ for Si, $2s^22p^5$ for F and $1s^1$ for H atoms. The force and energy convergence criteria were set to 0.05 eV Å^{-1} and 10^{-5} eV, respectively. A gamma-centred $2 \times 2 \times 1$ k-point grid was set in the Brillouin zone. The vacuum layer of the slab model was set to 15 Å to avoid the interaction between atoms in adjacent unit cells perpendicular to the surface.

Fabrication of inverted solar cells

ITO substrates were sequentially cleaned by detergent, deionized water and ethanol twice in an ultrasound cleaner. Before using them, they were dried under a N_2 flow and then treated in an ultraviolet–ozone oven for 30 min. First, ZnO nanoparticles (15 mg ml^{-1} in methanol) were spin coated on the ITO substrates at 3,000 r.p.m. for 30 s and then were annealed at 130 °C for 10 min. Sol–gel ZnO precursor solution was prepared by dissolving 148 mg of zinc acetate in 80 µl of ethanolamine and 1.5 ml of 2-methoxyethanol, and the sol–gel ZnO precursor solution was spin coated on the ITO substrates at 2,000 r.p.m. for 30 s, which were then annealed at 200 °C for 30 min. Then, PHPS (concentration from 0.01 to 0.1 vol% in DBE) was spin coated on top of the ZnO electron transportation layer at 3,000 r.p.m. for 30 s and kept in air (30% relative humidity; 25 °C) for 30 min. The mixed solution of PM6:Y6 with 0.5 vol% 1-chloronaphthalene was dissolved in chloroform with concentrations of 7.5 mg ml^{-1}, and the mixed solution of PM6:L8-BO (1:1.2 w/w) with 0.25 vol% of 1,8-diiodooctane was dissolved in chloroform with concentrations of 7.5 mg ml^{-1}. Then, PM6:Y6 and PM6:L8-BO was spin coated on top of the ZnO ETL at 2,500 r.p.m. for 60 s and then annealed at 130 °C for 10 min on a hot plate in a N_2-filled glove box. The solution of PM6:IT-4F (10 mg ml^{-1} for each compound) blended in chlorobenzene with 0.5 vol% 1,8-diiodooctane was spin coated on top of the ZnO electron transportation layer at 2,000 r.p.m. for 60 s and then annealed at 130 °C for 10 min on a hot plate in a N_2-filled glove box. Finally, MoO_3 (20 nm) as the hole extraction layer and Al (100 nm) as the anode were sequentially vacuum deposited on top of the active layer, respectively. The effective photovoltaic area, defined by the geometrical overlap between the bottom cathode electrode and the top anode, was 9 mm^2 and 100.17 mm^2. The small-area OSC was certified in the Shanghai Institute of Microsystem and Information Technology, Chinese Academy of Sciences (SIMIT), as ITO/ZnO/PHPS/PM6:L8-BO/MoO_3/Ag. The solutions of PM6:L8-BO (1:1.2 w/w, 15.2 mg ml^{-1} in total) in chloroform with 1,4-diiodobenzene as a solid additive (the content of 1,4-diiodobenzene is 50% of the total mass of the donor and acceptor) was stirred at 55 °C for 2 h. Then, PM6:L8-BO was spin coated and then annealed at 85 °C for 5 min on a hot plate in a N_2-filled glove box. All the ITO substrates we used for ZnO and SiO_xN_y-coated ZnO devices were the same.

Solar cell characterization

The photovoltaic parameters of the cells, including V_{OC}, J_{SC} and FF, were measured using a Keithley 2400 source meter under air mass 1.5 global (AM1.5G; 100 mW cm^{-2}) illumination provided by a solar simulator (Zolix SS150A) in a N_2-filled glove box at 25 °C. The cells are measured in the forward direction with a step of 0.02 V and the dwell time is 0.1 s for every point in our laboratory. The light intensity of the solar simulator for J–V measurement was calibrated with a reference silicon cell (QE-B1, Zolix). The designated illumination area defined by a thin metal mask of 5.77 mm^2 and 100.17 mm^2 was measured by a measuring microscope in SIMIT (report nos. 23TR060701 and 23TR021901).

The EQE spectra were recorded by a custom-built EQE system, and light from a 150 W tungsten halogen lamp (Osram 64610) was used as a probe light and was modulated with a mechanical chopper before passing through the monochromator (Zolix, Omni-k300) to select the wavelength. The response was recorded as the voltage by an I–V converter (D&R-IV converter, Suzhou D&R Instruments), using a lock-in amplifier (Stanford Research Systems SR830) with a standard silicon cell as the reference before testing the devices.

Degradation of polymer solar cells under white light

The long-term stability of unencapsulated devices was conducted by a multichannel solar cell performance decay test system (PVLT-G8001M, Suzhou D&R Instruments) in the glove box under testing conditions in accordance with the ISOS-L-1 protocol. The cells were put inside a N_2-filled glove box ($H_2O < 10$ ppm; $O_2 < 10$ ppm) and continuously illuminated with white LED illumination (D&R Light, L-W5300KA-150, Suzhou D&R Instruments). The illuminating light intensity was initially set such that the output J_{SC} matches that measured under standard conditions for AM1.5G illumination. Changes in the light intensity were monitored by a photodiode (Hamamatsu S1336-8BQ). $J–V$ characteristics of the devices were checked periodically, and the photovoltaic performance data (V_{OC}, J_{SC}, FF and PCE) were calculated automatically according to the $J–V$ curves. When the $J–V$ data were tested, the cell was attached to an external load matching the maximum power output point ($R_{mpp} = V_{max}/I_{max}$). Therefore, the device performance can be automatically recorded with time to monitor the $J–V$ curves. Because an external load can be changed with the $J–V$ results, the measured performance decay curves mean the performance decay behaviour of cells under real operation. Obviously, the results fully comply with the highest level of the ISOS-L-3 protocol (ref. 56). The temperature of the cells is thermostatically controlled at room temperature (25 °C) by temperature control equipment.

Device simulations

For the device simulations, a combined electro-optical model was used. The electrical behaviour is described by drift diffusion, accounting for the charge transport, recombination and space-charge effects inside the device[57]. The active bulk heterojunction layer is treated as an effective semiconductor sandwiched between the anode and cathode contacts. In the simulations, an active layer thickness of 105 nm, temperature of 300 K and dielectric constant of 3.5 were used, with an electron (hole) mobility of 4×10^{-4} cm^2 V^{-1} s^{-1} (2×10^{-4} cm^2 V^{-1} s^{-1}) and a 400 times reduced Langevin recombination rate[50]. The effective transport level gap and the effective densities of states were taken to be 1.22 eV and 10^{20} cm^{-3}, respectively[51]. Injection barriers of 70 meV and 100 meV were assumed for electrons at the cathode and holes at the anode, respectively. For devices without SiO_xN_y, a 15-nm-thick n-doped region with a fixed positively charged defect (doping) density of 5×10^{17} cm^{-3} was added at the cathode contact. For devices with SiO_xN_y, a reduced surface recombination velocity of 20 cm s^{-1} for holes at the cathode contact was used to account for the improved electron selectivity. Otherwise, non-selective contacts with high surface recombination velocities (10^6 cm s^{-1}) were assumed. The charge carrier photogeneration rate in the active layer is calculated using a transfer-matrix model accounting for optical interference effects[58]. Here the AM1.5G incident intensity spectrum, along with the refractive indices and extinction coefficients of all the layers in the device stack, is used as the input.

Reporting summary

Further information on research design is available in the Nature Portfolio Reporting Summary linked to this article.

Data availability

All data needed to evaluate the conclusions in this paper are present in the Article and its Supplementary Information. Source data are provided with this paper.

References

54. Beek, W. J. E., Wienk, M. M., Kemerink, M., Yang, X. & Janssen, R. A. J. Hybrid zinc oxide conjugated polymer bulk heterojunction solar cells. *J. Phys. Chem. B* **109**, 9505–9516 (2005).
55. Qian, L. et al. Electroluminescence from light-emitting polymer/ZnO nanoparticle heterojunctions at sub-bandgap voltages. *Nano Today* **5**, 384–389 (2010).
56. Reese, M. O. et al. Consensus stability testing protocols for organic photovoltaic materials and devices. *Sol. Energy Mater. Sol. Cells* **95**, 1253–1267 (2011).
57. Sandberg, O. J., Nyman, M. & Österbacka, R. Effect of contacts in organic bulk heterojunction solar cells. *Phys. Rev. Appl.* **1**, 024003 (2014).
58. Burkhard, G. F., Hoke, E. T. & McGehee, M. D. Accounting for interference, scattering, and electrode absorption to make accurate internal quantum efficiency measurements in organic and other thin solar cells. *Adv. Mater.* **22**, 3293–3297 (2010).

Acknowledgements

We acknowledge financial support from the National Natural Science Foundation of China grant nos. 22075315 (C.-Q.M.) and 22135001 (Q.L.) and Chinese Academy of Sciences grant no. YJKYYQ20180029 (C.-Q.M.). R.Ö. and C.-Q.M. would like to thank the Suzhou Science and Technology Bureau grant no. SWY2022004. Research Council of Finland is acknowledged through project no. 357196 (O.J.S.) and project no. 359833 (R.Ö.). We are grateful for technical support from the Vacuum Interconnected Nanotech Workstation (Nano-X), Suzhou Institute of Nano-Tech and Nano-Bionics, Chinese Academy of Sciences (A2107).

Author contributions

B.L. and C.-Q.M. conceived the idea and C.-Q.M. supervised the research. B.L. performed the device fabrication and characterization of OSCs with active areas of 5.77 mm^2 and 4 cm^2. B.L., J.Q., X.Y., W.Z. and N.W. performed the fabrication and characterization of cells with an active area of 100.17 mm^2. Y.L. and H.T. performed the DFT calculations. B.L. performed the TEM and AFM characterization and stability measurements of OSCs. J.F. performed the grazing-incidence wide-angle X-ray scattering characterization. B.L. and Z.L. performed the XPS and UPS characterizations. B.L. performed the inverse photoemission spectroscopy measurement of the SiO_xN_y film. B.L. and R.H. performed the TOF-SIMS characterization. O.J.S. performed and analysed drift–diffusion simulations. Q.L., C.-Q.M. and R.Ö. coordinated this work. B.L. wrote the first draft of the manuscript. S.W., R.Ö., O.J.S. and C.-Q.M. revised and finalized the manuscript. All the authors commented and approved the manuscript.

Competing interests

The authors declare no competing interests.

Additional information

Supplementary information The online version contains supplementary material available at https://doi.org/10.1038/s41566-024-01574-0.

Correspondence and requests for materials should be addressed to Qun Luo, Ronald Österbacka or Chang-Qi Ma.

Peer review information *Nature Photonics* thanks the anonymous reviewers for their contribution to the peer review of this work.

nature portfolio

Corresponding author(s): Chang-Qi Ma
Last updated by author(s): Sep 26, 2024

Reporting Summary

Nature Portfolio wishes to improve the reproducibility of the work that we publish. This form provides structure for consistency and transparency in reporting. For further information on Nature Portfolio policies, see our Editorial Policies and the Editorial Policy Checklist.

Statistics

For all statistical analyses, confirm that the following items are present in the figure legend, table legend, main text, or Methods section.

n/a	Confirmed	
☐	☒	The exact sample size (*n*) for each experimental group/condition, given as a discrete number and unit of measurement
☐	☒	A statement on whether measurements were taken from distinct samples or whether the same sample was measured repeatedly
☒	☐	The statistical test(s) used AND whether they are one- or two-sided *Only common tests should be described solely by name; describe more complex techniques in the Methods section.*
☒	☐	A description of all covariates tested
☒	☐	A description of any assumptions or corrections, such as tests of normality and adjustment for multiple comparisons
☐	☒	A full description of the statistical parameters including central tendency (e.g. means) or other basic estimates (e.g. regression coefficient) AND variation (e.g. standard deviation) or associated estimates of uncertainty (e.g. confidence intervals)
☒	☐	For null hypothesis testing, the test statistic (e.g. *F*, *t*, *r*) with confidence intervals, effect sizes, degrees of freedom and *P* value noted *Give P values as exact values whenever suitable.*
☒	☐	For Bayesian analysis, information on the choice of priors and Markov chain Monte Carlo settings
☒	☐	For hierarchical and complex designs, identification of the appropriate level for tests and full reporting of outcomes
☒	☐	Estimates of effect sizes (e.g. Cohen's *d*, Pearson's *r*), indicating how they were calculated

Our web collection on statistics for biologists contains articles on many of the points above.

Software and code

Policy information about availability of computer code

Data collection	DFT calculations were performed using the Vienna ab initio Simulation Package (Commercial software VASP, version 5.4.4) UPS and IPES were performed using the commercial softwares PHI smartsoft (version 3.2.0.52). TEM were performed using the commercial softwares Velox (version 2.14.0.703-125f3e7193).TOF-SIMS were performed using the commercial softwares SurfaceLab (version 6).
Data analysis	XPS and UPS were analysed by commercial software Themo Avantage (version 5.9921)

For manuscripts utilizing custom algorithms or software that are central to the research but not yet described in published literature, software must be made available to editors and reviewers. We strongly encourage code deposition in a community repository (e.g. GitHub). See the Nature Portfolio guidelines for submitting code & software for further information.

Data

Policy information about availability of data

All manuscripts must include a data availability statement. This statement should provide the following information, where applicable:

- Accession codes, unique identifiers, or web links for publicly available datasets
- A description of any restrictions on data availability
- For clinical datasets or third party data, please ensure that the statement adheres to our policy

All data needed to evaluate the conclusions in this paper are present in the Article or its Supplementary Information. Source data are provided with this paper.

Research involving human participants, their data, or biological material

Policy information about studies with human participants or human data. See also policy information about sex, gender (identity/presentation), and sexual orientation and race, ethnicity and racism.

Reporting on sex and gender	The study did not involve sex and gender.
Reporting on race, ethnicity, or other socially relevant groupings	The study did not involve race, ethnicity, or other socially relevant groupings .
Population characteristics	The study did not involve population characteristics .
Recruitment	The study did not involve recruitment.
Ethics oversight	HRP is not applicable to the study

Note that full information on the approval of the study protocol must also be provided in the manuscript.

Field-specific reporting

Please select the one below that is the best fit for your research. If you are not sure, read the appropriate sections before making your selection.

☐ Life sciences ☐ Behavioural & social sciences ☒ Ecological, evolutionary & environmental sciences

For a reference copy of the document with all sections, see nature.com/documents/nr-reporting-summary-flat.pdf

Ecological, evolutionary & environmental sciences study design

All studies must disclose on these points even when the disclosure is negative.

Study description	The study is about organic solar cells.
Research sample	Structure-inverted non-fullerene organic solar cells.
Sampling strategy	8 cells for each different types of solar cells were tested.
Data collection	The data was collected by the experimental test software.
Timing and spatial scale	Part of the experiment was from June 2021 to March 2023, and part of the experiment was from March 2023 to August 2024, spaced because some of the additional experiments responded to reviewer questions.
Data exclusions	Some solar cells were damaged during testing, so these data were excluded.
Reproducibility	We repeated the experiment at least 10 times, poor reproducibility of the experiment only once or twice.
Randomization	Each sample was randomly assigned and at least 8 solar cells were prepared for each condition in the same batch.
Blinding	The study is about solar cells which did not involve blinding.

Did the study involve field work? ☐ Yes ☒ No

Reporting for specific materials, systems and methods

We require information from authors about some types of materials, experimental systems and methods used in many studies. Here, indicate whether each material, system or method listed is relevant to your study. If you are not sure if a list item applies to your research, read the appropriate section before selecting a response.

Materials & experimental systems

n/a	Involved in the study
☒	☐ Antibodies
☒	☐ Eukaryotic cell lines
☒	☐ Palaeontology and archaeology
☒	☐ Animals and other organisms
☒	☐ Clinical data
☒	☐ Dual use research of concern
☒	☐ Plants

Methods

n/a	Involved in the study
☒	☐ ChIP-seq
☒	☐ Flow cytometry
☒	☐ MRI-based neuroimaging

Plants

Seed stocks	The study did not involve seed stocks.
Novel plant genotypes	The study did not involve novel plant genotypes.
Authentication	The study did not involve authentication.